Experimental study on characteristics of turbulence and sediment transport produced by wind-induced water waves

Sanjou, Michio
Department of Civil Engineering, Kyoto University

Sugihara, Yuji
Department of Advanced Environmental Science and Engineering, Kyushu University

出版情報：Physics of Fluids. 35 (2), pp.022111-1-022111-10, 2023-02-01. AIP Publishing
バージョン：

RESEARCH ARTICLE | FEBRUARY 23 2023

Experimental study on characteristics of turbulence and sediment transport produced by wind-induced water waves

M. Sanjou (山上路生) ; Y. Sugihara (杉原裕司)

Physics of Fluids 35, 022111 (2023)
https://doi.org/10.1063/5.0138538

Physics of Fluids ARTICLE scitation.org/journal/phf

Experimental study on characteristics of turbulence and sediment transport produced by wind-induced water waves

Cite as: Phys. Fluids **35**, 022111 (2023); doi: 10.1063/5.0138538
Submitted: 13 December 2022 · Accepted: 1 February 2023 ·
Published Online: 23 February 2023

M. Sanjou (山上路生),[1,a] and Y. Sugihara (杉原裕司)[2,b]

AFFILIATIONS

[1]Department of Civil Engineering, Kyoto University, Kyoto 6158540, Japan
[2]Department of Advanced Environmental Science and Engineering, Kyushu University, Kasuga 8160811, Japan

[a]Author to whom correspondence should be addressed: sanjou.michio.6c@kyoto-u.ac.jp
[b]Electronic mail: sugihara.yuji.290@m.kyushu-u.ac.jp

ABSTRACT

Many researchers and engineers have shown great interest in mass transfer processes produced by wind-induced waves. Such waves contribute significantly to the transfer of environmental materials, such as sediment and marine debris, and the turbulence occurring beneath the waves further complicates wave-induced mass transport. The phase cycle of wave motion is generally considered to be a key determinant of mean flow and turbulence. In aqueous environmental engineering, this relationship is a crucial one to investigate, since turbulence is closely related to mass transport. To address this question, we measured the time-series of instantaneous velocity vectors by means of particle image velocimetry in a laboratory flume to reveal the turbulence structure induced by wave motion. By using a wavelet analysis free of specific assumptions, we were able to decompose the instantaneous velocity data into mean current, wave motion, and turbulence components. This analysis allowed for the objective evaluation of the shear stresses related to wave energy and turbulence energy production. Furthermore, we found significant phase characteristics of energy transfer among mean velocity, wave, and turbulence components. In order to examine the diffusion and convection properties induced by wind waves, we also conducted tracking analysis of imaginary sediment markers. Our results support the conclusion that mass transfer induced by wind waves impacts the entire range of water depths, at least in relatively shallow aqueous environments.

I. INTRODUCTION

Wind-induced water waves play an important role in mass and momentum transfer in natural lakes and oceans. Hence, many researchers have shown interest in this phenomenon. Proper sediment control and prediction are required to prevent the retreat of sandy beach. Excessive sedimentation in estuary causes inundation of river flow. In contrast, estuary sediments block the invasion of salt water from the coastal zone. Therefore, excavation for flood control will cause environmental problems. Thus, sediment transport is related to rivers and coastal areas. Hence, we need to consider sediment dynamics for both areas in a well-balanced manner. Colosimo *et al.* (2020) measured waves and sediment concentrations on an intertidal flat. They suggested that sediments can be temporarily stored in the shallower areas of the intertidal system, and then, it is easy for them to be resuspended and advected during wind events. Some researchers have reported the influences of wind waves on sediment transport in lakes. For example, Lin *et al.* (2021) reported that sediment resuspension is more promoted by the wind waves in the shallower zone. Zainescu *et al.* (2023) considered numerically the hydro-sedimentary dynamics of Lake Turkana, and they claimed the impact of wind in generating wind waves responsible for the resuspension and redistribution of fine sediment at lake basin scale.

Presently, engineers are interested in millimeter-sized marine debris called "micro-plastic," which is globally distributed and diffused throughout the ocean (e.g., Kukulka *et al.* 2012; Khanhai *et al.* 2017; Law 2017; Auta *et al.* 2017; Brach *et al.* 2018; Pellini *et al.* 2018; and DiBenedetto *et al.* 2018). This major pollutant is a threat to the natural environment. As majority of these plastic fragments have a density similar to that of water, ongoing natural processes degrade them slowly. Thus, these particles travel long distances, subject to current and turbulence beneath wind-induced waves at the surface. Using a one-dimensional theoretical model in conjunction with observational

data, Kukulka *et al.* (2012) demonstrated the vertical mixing of microplastics caused by wind shear stress.

Accurate predictive mass transfer models for such sand sediment and marine debris require reliable knowledge of hydrodynamics beneath wind-induced waves. Adequate knowledge of shear stress promoted by waves is required as it is closely related to energy dissipation of waves and momentum transfer. Deigaard and Fredsoe (1989) focused on the contribution of the horizontal orbital motion to the vertical mass transfer, developing theoretical models to relate energy flux with shear stress. Nielsen *et al.* (2011) proposed a theoretical model of momentum transfer in growing waves. Rivero and Arcilla (1995) related the effective wave shear stress to two-component normal stresses and vorticity, providing a theoretical equation describing the vertical profile of wave shear stress. Mellor (2013) developed analytical models for pressure-slope vertical momentum transfer induced by gravity waves. Sanjou and Nezu (2011) found that waves influence the structure of bottom-oriented turbulence.

In the context of the above-mentioned studies, it is important to acknowledge the connection between orbital motion and turbulent fluctuation. Because of this connection, it is crucial to separate background turbulence, which contributes significantly to diffusive mass transfer. Several previous studies have proposed promising methods for accomplishing this decomposition; we have reviewed a few here.

Hussain and Reynolds (1970) developed a "phase-averaging technique" to decompose the instantaneous velocity component into mean, turbulence, and wave motion components. In the last three decades, various methods were suggested for improving this technique. Cheung and Street (1988) used a linear filtering technique (LFT) in which wave motion is evaluated by the cross-spectra of velocity and free-surface fluctuation. This technique showed a significant energy transfer from waves to the mean flow. Furthermore, the aqueous turbulence structure induced by wind waves in their study had characteristics similar to those observed in turbulence boundary layers.

Jiang *et al.* (1990) proposed a stream function method (SFM). They revealed that the interaction between wave and turbulence plays a vital role in the energy transfer mechanism. By considering the turbulence kinetic energy (TKE) equation, they proposed a generation term comprising the turbulent Reynolds stress term and wave–turbulence interaction term. Their measurement data demonstrated that the mean current supplies energy to the turbulence based on the sign of the Reynolds stress term in the TKE equation. Meanwhile, energy transfer from the turbulence to the mean current depends on the sign of the wave–turbulence interaction term. The sum of the generation term and wave–turbulence interaction term, i.e., net energy transfer, depends on the wind speed. In other words, energy is transferred from the turbulence to the mean current at low wind speeds, whereas it is transferred from the mean current to the turbulence at high wind speeds. They also found that the mean current supplies energy to the waves.

Kato *et al.* (2002) applied SFM to a closed channel with wind-induced waves and suggested that turbulence increases more at the trough than at the crest. A combined SFM–LFT method was proposed by Thais and Magnaudet (1996). Such decomposition techniques enable us to consider the energy transfer mechanisms and interactions between the mean current, wave, and background turbulence. They assumed that when the vortex timescale is sufficiently small compared to the wave period, small vortices exist throughout the depth, and the energy transfer from the wave to the turbulent vortex is limited to a specified energy scale. In contrast, when the vortex timescale is much larger than the wave period, energy transfer is not expected as the turbulence fluctuation is almost frozen compared to the wave motion. Moreover, they demonstrated that the most significant interactions between turbulence and waves occur when the turbulence timescale is equal to the wave period. Furthermore, their experiments showed that the waves supplied energy to turbulence via the mean current, i.e., water waves generate turbulence in excess. Nielsen *et al.* (2011) claimed that wave-induced Reynolds stress term is generated when the waves grow or decay in the streamwise direction. Longo *et al.* (2012a, 2012b) evaluated micro- and macro-scales of turbulence structures induced by wind waves. Clavero *et al.* (2016) conducted 3D flow measurement using the 3D-PTV technique. They showed that turbulence kinetic energy (TKE) is essential in the cross-shore and vertical directions in the regular breaking waves. Chiapponi *et al.* (2017) investigated the vorticity generation mechanism in the breaking waves by quantifying the terms in the vorticity equation. Longo *et al.* (2017) analyzed the anisotropy of the Reynolds stress and dissipation tensors in the breaking waves. They elucidated that the anisotropy, which is quantified by the invariants, is relatively high during all phases and more evident for the most energetic breakers. Olfateh *et al.* (2017) used laboratory experiments to examine the effects of reflection waves on the decomposed cross-correlation stress. They concluded that difference in the wave-tank condition causes inconsistent results for the wave-induced Reynolds stress in previous experiments. Addona *et al.* (2018) pointed out that reflection waves promote the modulation of wave-induced Reynolds stress which becomes much larger than the turbulent Reynolds stress. Furthermore, Addona *et al.* (2020) reported the effects of partially reflected regular waves under the action of an opposite wind. Chiapponi *et al.* (2020) conducted experimental analysis to reveal the interaction between wind waves and currents in a wind-wave-current tunnel. They concluded that energy transfer and breaking are significantly affected by currents. Nove-Josserand *et al.* (2020) have numerically investigated the influence of a weak current on wind-generated surface deformations for wind velocity below the onset of regular waves.

However, there exists no consensus regarding wave-induced mass transfer properties beneath the free-surface. Therefore, we focus on the following topics through laboratory measurements using a particle image velocimetry (PIV) system:

1. The hydrodynamic effects of wind-induced waves on mean flow profiles near the air–water interface.
2. The separation of the turbulence and wave fluctuation components using the wavelet analysis.
3. The evaluation of wave-induced turbulence production and interaction between wave and turbulence components.
4. The phase properties of turbulence and wave energy generation.
5. The analysis of sediment transport caused by convection and diffusion beneath water waves.

This paper is organized as follows: In Sec. II, we describe the experimental procedures for velocity measurements and the method to extract background turbulence. In Sec. III, the turbulence structure is considered based on the measurement results and the relationship between the phase cycle and energy transfer direction is discussed. In Sec. IV, we examine the diffusion and convection properties of

sediment induced by wind waves based on the tracking analysis of imaginary markers. In Sec. V, we propose a phenomenological model based on the present results. Our conclusions are described in Sec. VI.

II. EXPERIMENTAL PROCEDURE AND ANALYTICAL METHOD

A. Experimental setup

The experimental setup is shown in Figs. 1(a) and 1(b). The experiments were conducted in a 16 m long, 40 cm wide, and 50 cm high glass wind tunnel-flume. The bottom is made of glass, and the flow can be visualized by a laser light from below. In this flume, airflow was generated over the water layer by a speed-controlled fan. The fan can generate wind speeds of more than 10 m/s. At the downstream-edge, a wave diffuser was placed to prevent reflection waves. The reflection coefficient evaluated using the Healy formula was approximately 0.15 in the present hydraulic condition. x and y represent the streamwise and upward vertical coordinates, respectively, and y' is the downward vertical coordinate based on the free-surface. The vertical origins, $y = 0$ and $y' = 0$, were chosen as the channel bed and static free-surface, respectively. The time-averaged velocity components in the x, y, and z directions are defined as U, V, and W, and the corresponding fluctuations as u, v, and w, respectively. H represents static water depth, and η represents the fluctuation of the free-surface height. Measurements were conducted 7 m downstream from the channel entrance.

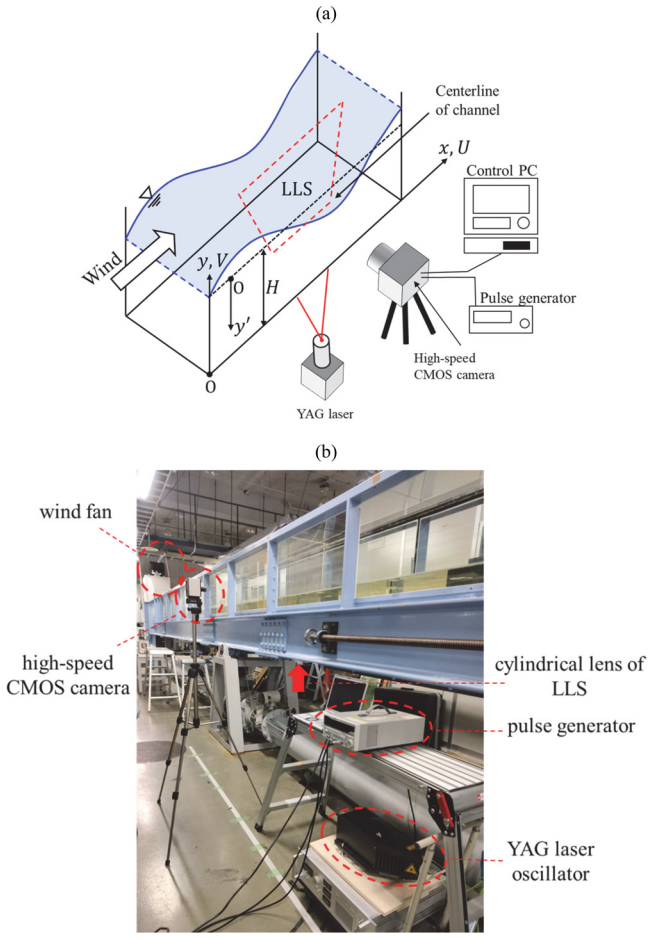

FIG. 1. Experimental setup: (a) PIV measurements in a laboratory flume with coordinate system and (b) photograph of the instruments and the wind tunnel flume.

A 2 W YAG laser light sheet (LLS) was projected from the flume bottom. The thickness of LLS is approximately 2 mm. The tracer particles in the $x - y$ plane were illuminated with the LLS, and images were captured using a high-speed CMOS camera (DITECT HAS-500 with the maximum frame rate of 4000 Hz). The number of effective pixels was set to be 1024 × 992. The high-speed CMOS camera was connected to a pulse-signal generator. A trigger signal with the same frequency as the 50 Hz data sampling rate was transferred to the CMOS camera via the control computer, and a pair of digital images were taken at the 100 Hz frame rate of the CMOS camera.

The time variation of the instantaneous velocity vectors $(\tilde{u}, \tilde{v})$ was calculated using the PIV algorithm below the mean trough level, i.e., $y < 0.94H$—in other words, $y' > 0.06H$. Table I shows the hydraulic conditions under which the static water depth H was fixed at $H = 4.2$ cm. The free-surface velocity U_s was evaluated using Eq. (5), as shown by Wu (1975).

The maximum wind speed $U_{a,\max}$ was measured by hot-wire velocimetry (Testo, model 425), and thus also fixed. U_* represents the friction velocity of the water current near the free-surface, as evaluated by the log-law. f_p represents the frequency of the peak spectrum of water wave fluctuations measured by the wave gauge. Finally, H_s is the significant wave height. In this case, 2D gravity waves were observed. The error bars in figures in Sec. III are based on the standard deviation of five measurements.

B. Decomposition technique of instantaneous velocity

As mentioned previously, several useful methods have been developed for decomposing instantaneous velocity data into wave and background turbulence components. Wavelet analysis is often used to compare the time-series of measured data in different frequency bands (e.g., Farge 1992). Unlike standard spectral analysis, wavelet analysis allows frequency to be analyzed without information on time variation. Moreover, wavelet analysis requires no further assumptions that other decomposition methods demand. For example, LFT requires the specific condition that wave motion and turbulence show zero correlation. Therefore, in this study, we used discrete wavelet analysis, which yields copious time-series data in frequency bands lower than the sample rate. By applying the present technique to the measured data with a sampling frequency of 50 Hz, we obtained the time variations of velocity components in the following frequency bands: 25–50, 12.5–25, 6.25–12.5, and 3.125–6.25 Hz. The peak wave frequency was approximately $f_p = 2.49$ Hz, as shown in Table I. Therefore, we defined wave motion as motion with a frequency less than 3.125 Hz.

TABLE I. Hydraulic conditions.

H (cm)	$U_{a,\max}$ (m/s)	U_s (cm/s)	U_* (cm/s)	f_p (Hz)	H_s (cm)	H_s/H
4.2	6.8	15.8	1.00	2.49	0.40	0.1

Instantaneous velocity $\tilde{u}$ can be decomposed into time-averaged velocity U, velocity associated with wave motion u_w, and turbulence u_t in the following form:

$$\tilde{u} = U + u_w + u_t \quad . \tag{1}$$

III. CURRENT PROPERTIES BENEATH WATER WAVES

A. Mean velocity profiles

Figure 2 shows the vertical profiles of time-averaged streamwise velocity. We can observe a return flow $U < 0$ under $y/H = 0.15$ and a large velocity gradient $\partial U/\partial y$ near the free-surface, $y/H > 0.2$. Near the flume bed $y/H = 0$, the velocity decreases because of bottom friction. Velocity shear is much larger in the free-surface than that at the flume bottom. Hence, greater turbulence is expected to be produced by the wind stress than by the bottom-oriented boundary layer.

Figure 3 shows the velocity profiles normalized by inner variables. The following roughness log-law used by Longo *et al.* (2012a) was then fit to the measured data:

$$U^+ = \frac{1}{\kappa}\ln y'+ + A, \tag{2}$$

where $U^+ = (U_s - U)/U_*$, $\kappa = 0.412$, and $A = 5.5$. $y'+ = y'U_*/\nu$ is the normalized height with kinematic viscosity ν. The resulting fit suggests that the log layer exists, i.e., the normalized velocity profile corresponds to Eq. (2). The interfacial friction velocity of the water current U_* could be evaluated using this fitting process. The counter-current appearing in the lower layer causes the difference between the velocity profile and the log-law. Thus, Eq. (2) describes processes quite similar to those observed in the wall boundary layer in an open channel. This means that not only the wall boundary layer but also the water waves themselves play a significant role in producing frictional force and related turbulence.

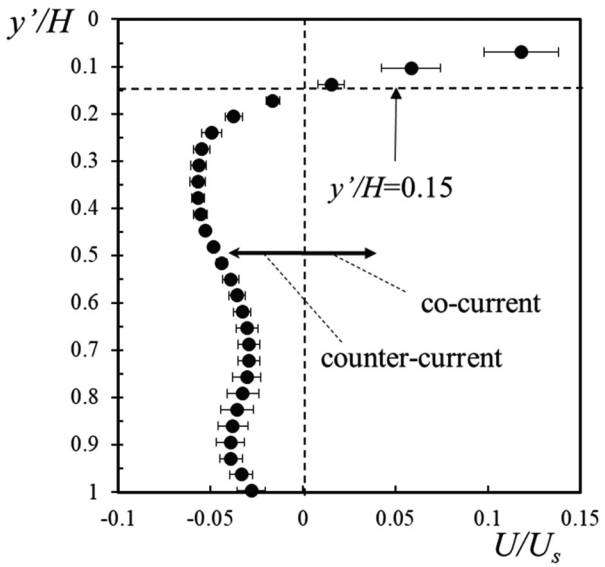

FIG. 2. Vertical profile of the streamwise mean velocity.

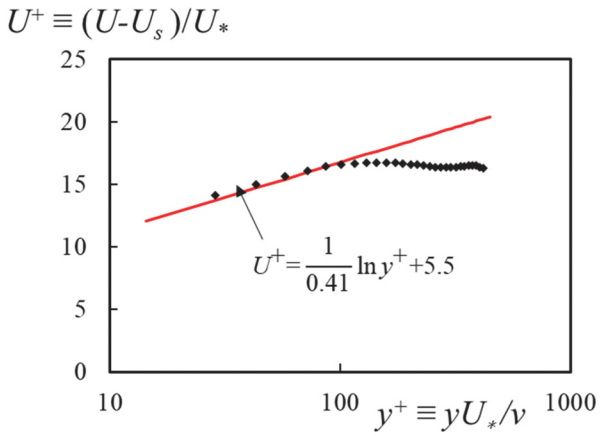

FIG. 3. Profile of the streamwise velocity normalized by inner variables.

B. Properties of decomposed velocity components

Figure 4 shows the profiles of streamwise and vertical turbulence intensities, i.e., u_t' and v_t', respectively. The results decomposed by the LFT method (Jiang *et al.* 1990) are also included for comparison. The turbulence intensities are normalized by the friction velocity U_*, and the vertical axis is normalized by the boundary layer thickness δ at which turbulence shear stress vanishes (see below). u_t' and v_t' tend to decrease with increasing depth, in agreement with the experiment of Jiang *et al.* This suggests that significant turbulence is produced near the air–water interface through the interaction between the maximum mean currents and water waves.

Reynolds stress was decomposed into four components as follows:

$$-\overline{uv} = -\overline{u_w v_w} - \overline{u_t v_t} - \overline{u_w v_t} - \overline{u_t v_w}, \tag{3}$$

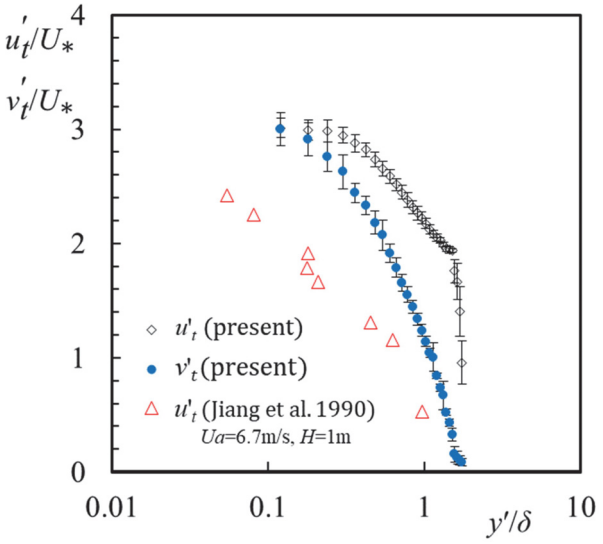

FIG. 4. Vertical profiles of the turbulence intensity after the decomposition procedure.

where each overbar signifies a time-averaged operation. Therefore, energy loss $E = \overline{uv}\partial U/\partial y$ in the energy transport equation for the mean current can be written as follows:

$$E = (\overline{u_w v_w} + \overline{u_t v_t} + \overline{u_w v_t} + \overline{u_t v_w}) \times \partial U/\partial y. \quad (4)$$

When a negative sign is applied to the first and third terms on the right-hand side of this equation, we obtain $(-\overline{u_w v_w} - \overline{u_w v_t})\partial U/\partial y$, which is the production term in the transportation equation of wave kinetic energy (WKE) (Jiang *et al.*, 1990). Particularly, $-\overline{u_w v_w}\,\partial U/\partial y$ denotes the energy supply from the mean current to the wave field. The second and fourth terms become $(-\overline{u_t v_t} - \overline{u_t v_w})\partial U/\partial y$, which is the production term in the TKE equation. $-\overline{u_t v_t}\,\partial U/\partial y$ denotes the energy supply from the mean current to the turbulence field. Hence, evaluating the sign of these terms allows us to understand the direction of energy transport among the mean current, wave, and turbulence.

Figure 5 shows a vertical profile of normalized turbulence Reynolds stress $-\overline{u_t v_t}/U_*^2$, in which the measured data of Thais and Magnaudet (1996) are also plotted for comparison. In the present study, we extracted a pure turbulence component from the raw velocity data. This results in the present turbulent Reynolds stress following a linear profile similar to that of Thais and Magnaudet.

$$-\overline{u_t v_t}/U_*^2 = 1 - y'/\delta. \quad (5)$$

Equation (5) implies consistency of the friction velocity obtained from the log-law [Eq. (1)] and that obtained from the linear profile of Reynolds stress [Eq. (5)].

Figure 6 shows a vertical profile of normalized wave Reynolds stress $-\overline{u_w v_w}/U_*^2$, in which the measurement data of Cheung and Street (1988) and Thais and Magnaudet (1996) are included for comparison. This figure shows that the wave Reynolds stress varies significantly in the free-surface region. Indeed, where Cheung and Street's method might obtain a negative stress, Thais and Magnaudet's method might obtain a positive stress. Although the present study obtained a negative peak, supporting Cheung and Street's result, the phase lags of u_w and v_w seem to define the sign of cross-correlation, i.e., $-\overline{u_w v_w}$. The determination of the peak may depend on the experimental setup and analytical method.

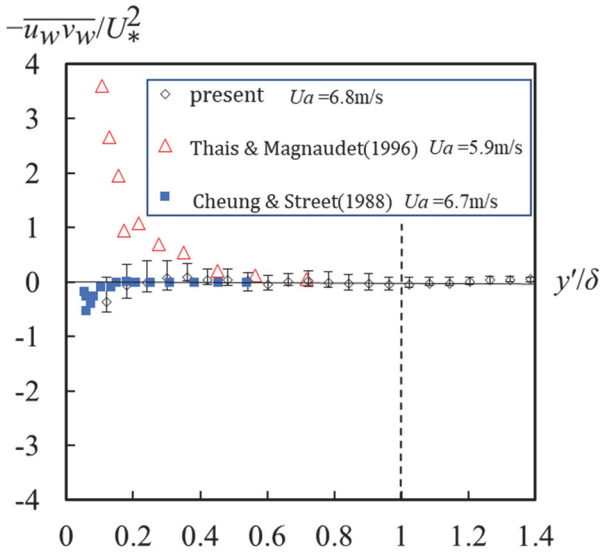

FIG. 6. Vertical profiles of the wave component of Reynolds stress normalized by friction velocity.

The wave Reynolds stress is asymptotically approaching zero at $y'/\delta = 0.2$–0.5—shallower than the decay of the turbulence Reynolds stress $-\overline{u_t v_t}/U_*^2$ (Fig. 5).

Figure 7 shows the vertical distributions of the turbulence Reynolds stress $-\overline{u_t v_t}/U_*^2$, wave Reynolds stress $-\overline{u_w v_w}/U_*^2$, and turbulence–wave correlation components $-\overline{u_w v_t}/U_*^2$ and $-\overline{u_t v_w}/U_*^2$. It can be observed from Fig. 7 that $-\overline{u_w v_w} < 0$ and $-\overline{u_t v_t} > 0$ are observed near the free-surface. As $\partial U/\partial y$ is positive in the free-surface region, wave fluctuation supplies kinetic energy to the mean current. Meanwhile, the mean current supplies kinetic energy to the

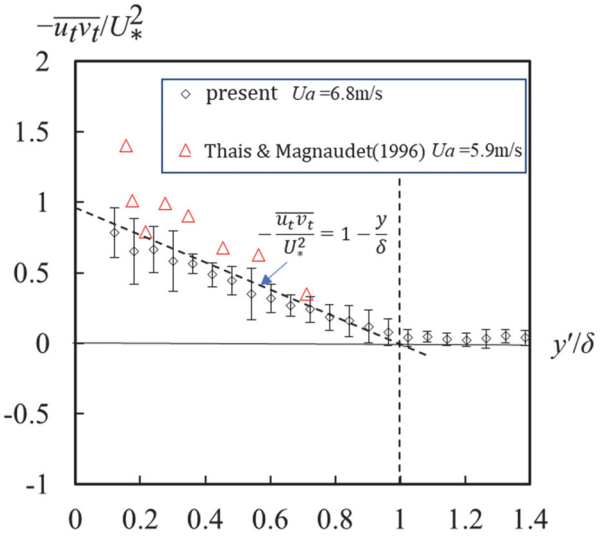

FIG. 5. Vertical profiles of the turbulence component of Reynolds stress normalized by friction velocity.

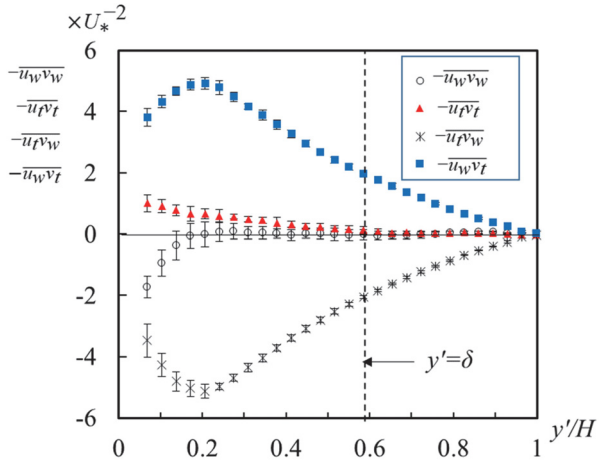

FIG. 7. Comparison of decomposed Reynolds stress components.

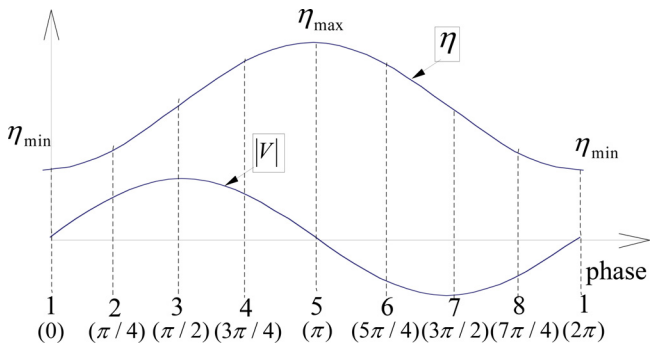

FIG. 8. Phase definition based on wave cycle.

turbulence. This results in the waves supplying energy to the turbulence via the mean current. Hence, waves are expected to exert significant influence on the turbulence structure.

The wave–turbulence correlation terms are much larger in magnitude than the turbulence and wave Reynolds stress. Although there is no direct turbulence transfer between the turbulence and wave fields, these fields contribute significantly to the production and dissipation of kinetic energy. A positive $-\overline{u_w v_t}$ value near the free-surface denotes energy production of the wave field, whereas a negative $-\overline{u_t v_w}$ value near the free-surface means energy dissipation of the turbulence field.

C. Phase analysis

Waves contribute significantly to turbulence production near the free-surface. Therefore, it is important to conduct phase analysis to understand how wave motions affect the mean flow and turbulence at each phase of the wave cycle. As the time-cycle of velocity near the free-surface corresponds to the time variation of free-surface height, the wave component of vertical velocity at the mean trough level was used for defining the phase. Figure 8 shows a sketch of phase definition. One wave cycle was divided into eight phases. The trough denotes the transition at which the sign of the vertical velocity changes from negative to positive. Phase number 1 shows this transition. Another transition from positive to negative denotes the crest, i.e., phase number 5. We evaluated ensemble-averaged quantities for each phase.

Figure 9 shows the phase variation of the phase-averaged velocity vectors and contours of streamwise velocity. A rising stage occurs during phases 2–4. In contrast, a falling stage occurs during phases 6–8. Rotational motion around a spanwise axis is observed corresponding to waves. The small streamwise phase-averaged velocity was recorded near the free-surface in the trough phase. Thus, the mean current structure varies significantly with the phase cycle.

Figures 10(a) and 10(b) show the phase cycles of turbulence and wave production terms, respectively. Here, we compare the results of near free-surface $y'/H = 0.172$ and mid-depth $y'/H = 0.584$. The turbulence production term near the free-surface takes a positive value at the trough, and it is larger than that observed at the crest. This suggests that significantly more TKE tends to be produced at the trough than that at the crest, in agreement with the results of Kato *et al.* (2002). Particularly, we observe significantly negative turbulent production in the depth-falling phase following the crest. Notably greater variation is observed at the free-surface compared to the mid-depth.

By contrast, the wave production term near the free-surface is positive at the crest and trough. The negative production is significantly observed in the rising and falling phases. We found that the phase properties of the turbulence production term are quite different from those of the wave energy production term. Thus, the energy transfer direction varies with the phase cycle, as indicated in Table II.

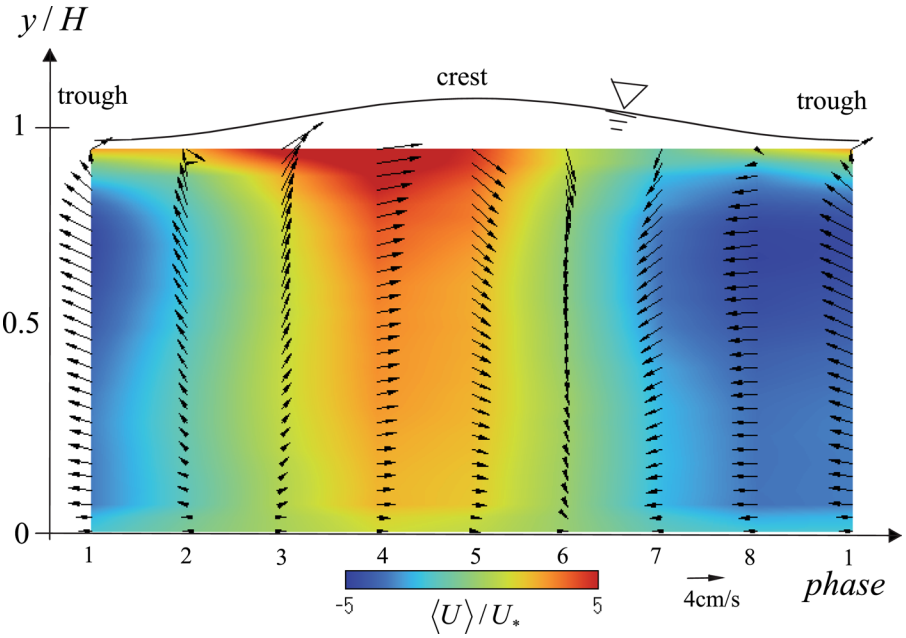

FIG. 9. Phase variation of phase-averaged velocity vectors, in which color denotes streamwise velocity.

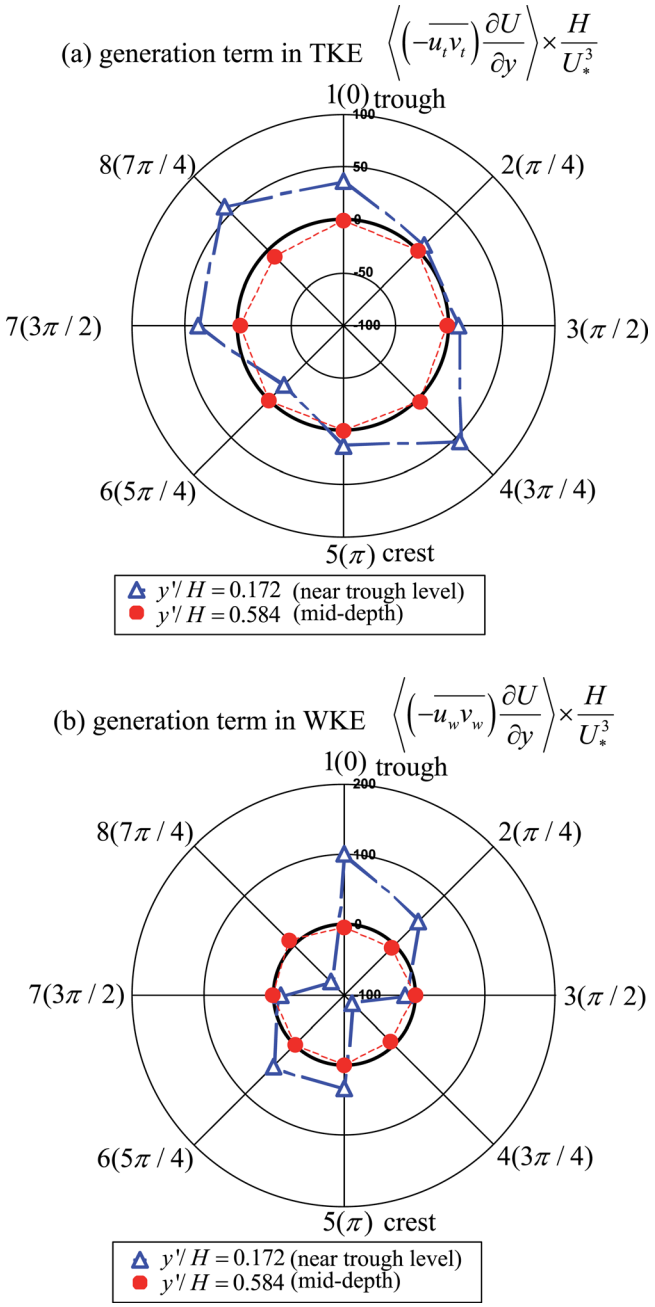

FIG. 10. Phase cycles of the energy generation term at different elevations: (a) in the turbulence kinetic energy equation (TKE) and (b) in the wave kinetic energy equation (WKE).

IV. SEDIMENT TRANSPORT INDUCED BY WAVES

In the management of lake and ocean environments, it is crucial to understand mass transport and diffusion properties. Laboratory experiments have often used point measurements to evaluate these properties by means of concentration sensors or dye visualization. Particularly, a laser-induced fluorescence method can be used to quantify how the turbulence brings about mass transport (e.g., Okamoto *et al.* 2012).

TABLE II. Relation between the phase cycle and energy transfer direction.

Phase	Directions of energy transfer
trough	Mean → Wave, Mean → Turbulence
rising (trough → crest)	Mean ←→ Wave, Mean → Turbulence
crest	Mean → Wave, Mean → Turbulence
falling (crest → trough)	Mean ←→ Wave, Mean← → Turbulence
in total	Mean ← Wave, Mean → Turbulence

However, these experiments have their own problems. For instance, the use of a two-dimensional measurement makes it challenging to completely capture the three-dimensional dye diffusion. Furthermore, it is difficult to project LLS with constant brightness in the illuminated plane. Therefore, in the present study, we took a different approach. As spanwise diffusion is assumed to be much smaller than diffusion in longitudinal and vertical directions, we applied a Lagrange tracking method.

In this study, we target very fine sand, such as silt. For example, with the sediment density of $\rho_s = 1600$ kg/m^3, sediment diameter of $d_s = 10^{-5}$ m, viscosity of $\mu = 10^{-3}$ kg/ms, U_s on the velocity scale, and H on the length scale, Stokes number $S_t \equiv \frac{\rho_s d^2 U_s}{18\mu H}$ was calculated to be 6×10^{-4}. As this value is sufficiently smaller than 1, it can be considered that the followability of the imaginary sediment to the flow is large, and the influence of inertia and settling velocity of the sediment is sufficiently small to be ignored. Therefore, in this calculation, the local flow velocity was given as the moving velocity of the imaginary sediment. In this method, a time-series of spatial position of imaginary sediment markers was calculated from the instantaneous velocity component obtained in the present PIV experiment.

Figure 11 shows the trajectories for four markers every 0.02 s over a duration of 20 s, with initial marker elevations of $y_i/H = 0.2$, 0.4, 0.6, and 0.8, respectively. The four markers were released simultaneously. The initial time corresponds to the trough phase of the wave,

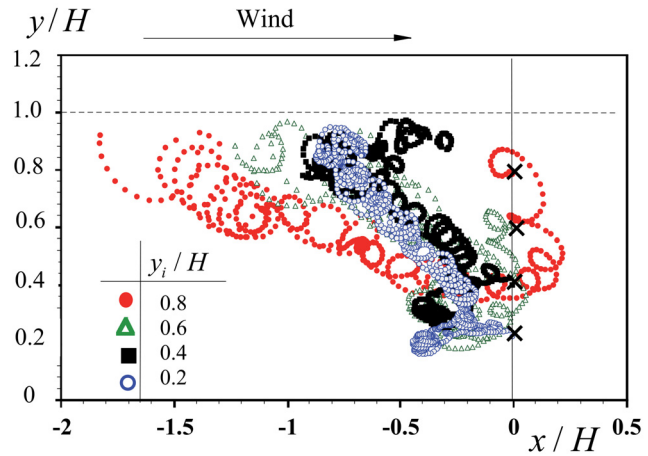

FIG. 11. Trajectory lines of imaginary particles in a two-dimensional vertical plane.

resulting in a rising motion with clockwise rotation. The marker released near the bottom at $y_i/H = 0.2$ was also found to show this tendency because of the comparatively small depth in this experimental case. After this initial motion, the markers had cyclical trajectories.

The marker released near the free-surface was transported upstream and went down to the countercurrent elevation ($y/H = 0.4$). This may have been due to a sudden strong downward turbulence, i.e., down bursting. Furthermore, after downward transportation, the marker went up toward the free-surface. In the near-surface region, the high-speed current accelerated the markers significantly. The marker released near the bottom also experienced a rising motion toward the free-surface, again with clockwise rotation. These results suggest that mass transfer by wind waves affects the entire range of water depths, at least in comparatively shallow depths like those of the experiment.

We also need to undertake a quantitative consideration of relative diffusion properties, estimating the diffusion coefficient from the time variation of two different markers. In this simulation, three kinds of initial release elevations were chosen: $y_i/H = 0.25$, 0.5, and 0.9. An initial distance between the two markers was set at $Y_r(0)/H = 0.0005$. After 300 trials at varying initial phase, an ensemble-averaged distance $\overline{Y_r}(t)$ was calculated. Figure 12 shows the time-series of $\overline{Y_r}(t)$, where t denotes diffusion time. Near the free-surface, the final distance between the two particles was found to be larger. We ascribe this tendency to the strong turbulence in the free-surface region (Fig. 4).

Figure 13 shows the relationship between the diffusion distance and the degree of the corresponding fitting power function. When the diffusion time is short, the diffusion distance is proportional to the elapsed time. Subsequently, the diffusion distance is proportional to the 3/2nd power of elapsed time. This time region corresponds to the inertial region in Richardson's law, in which the diffusion coefficient is proportional to the 4/3rd power of the diffusion length scale, i.e., the distance between the two markers. As diffusion progresses further, the distance between the two markers becomes larger than the maximum vortex scale. This results in a proportionality to the 1/2 power of time, and therefore close to a constant value. In the case of $y_i/H = 0.5$, the inertial region appears 1.8–6.4 s after the release. As the release elevation approaches the free-surface, the diffusion scale rapidly approaches the vortex scale.

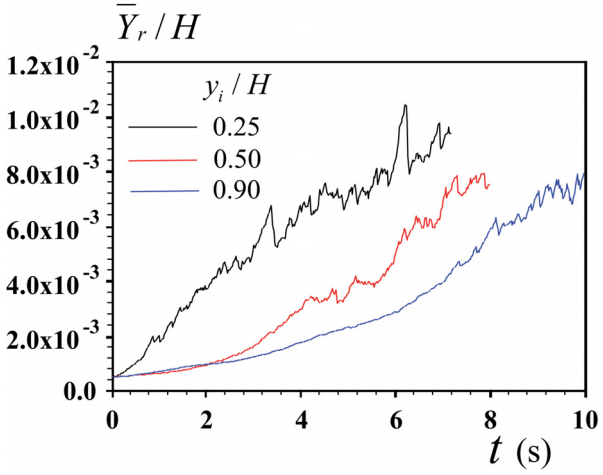

FIG. 12. Time variation of the instantaneous distance between two particles.

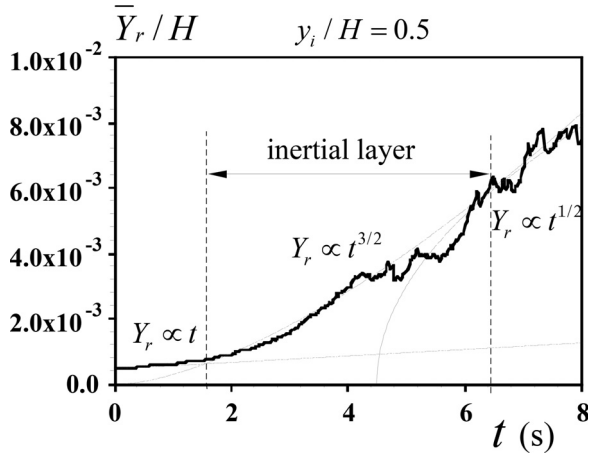

FIG. 13. Inertial layer of the relative diffusion process.

If the size of the sediment is larger, the motion equation of the sediment particle must be used together to obtain reliable results. We would like to leave this as an issue for the future.

V. PHENOMENOLOGICAL MODEL

Figure 14 shows a proposed phenomenological model based on the present results. The wind accelerates the free-surface current and induced velocity shear near the free-surface. The countercurrent is observed near the bottom in the closed zone, as in the case of a lake or pond. This mean flow property is not related to free-surface variation. Wind-induced water-waves generate the energy transport among the mean current, waves, and turbulence, and the transport direction varies with the phase of the wave as discussed above.

Rashidi and Banerjee (1990) experimentally revealed the turbulence structure near the free-surface in wind-driven currents and pointed out the existence of low- and high-velocity streaks even in the free-surface layer. From this evidence, they inferred that the air–water interfacial boundary layer has fluid dynamics similar to those of the wall boundary layer. We aim to reveal more about this mechanism and its physical basis through further analysis, namely, energy budgets in wave and turbulence transport equations.

Mass transport is composed of two components: convection by wave motion and turbulent diffusion. In comparison with open-channel flow, in which streamwise transport is predominant, the matter in wave motion remains in rotational motion corresponding to the waves. Furthermore, in the context of Richardson's relative diffusion theory, wave motion also promotes turbulence diffusion in the inertial region. The present model will be also useful in the progress of the research works on heat and gas transfer in the free-surface flow, e.g., Sanjou *et al.* (2017), Szeri (2018), Herlina and Wissink (2019), Sanjou (2020), and Tseng and Tinoco (2020).

VI. CONCLUSIONS

The present study highlights the turbulence structure and energy transport under the presence of wind-induced waves and reveals the related mass transfer caused by local turbulence diffusion and convection.

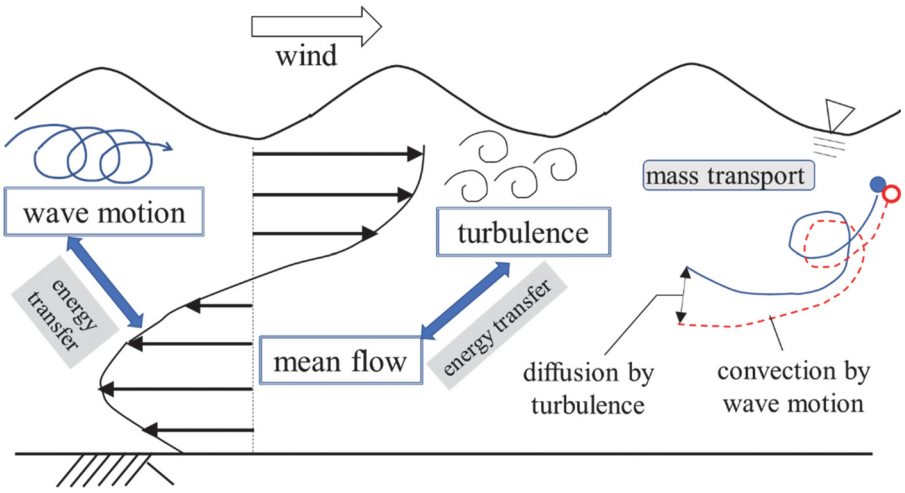

FIG. 14. Phenomenological model of mass transport beneath water waves.

The main findings of this study are summarized below:

(1) In a wavelet analysis free of specific assumptions, we decomposed the time-series of instantaneous data and evaluated the wave component, turbulence component, and turbulence–wave correlation component of shear stress, in comparison with previous studies.
(2) By evaluating the energy generation terms appearing in the mean current kinetic energy equation (MKE), in the turbulence kinetic energy equation (TKE), and in the wave kinetic energy equation (WKE), we examined the energy transfer properties among the mean current, wave motion, and turbulence. We found that wave motion supplied kinetic energy to turbulence via the mean current. We therefore expect waves to exert significant influence on the turbulence structure.
(3) Phase analysis showed that turbulence was produced significantly more in the depth-rising stage, i.e., from the trough to the crest, than in the depth-falling stage, i.e., from the crest to the trough. By contrast, the wave production term near the free-surface took a positive value at the crest and trough, but took a negative value at other phases. We found that the phase properties of the turbulence production term were quite different from those of the wave energy production term.
(4) Applying a Lagrange tracking method, we calculated the time-series of spatial positions of imaginary markers. Released markers experienced a rising motion toward the free-surface, with clockwise rotation. These results suggest that mass transfer by wind-waves affects the entire range of water depths, at least in comparatively shallow depths like those of the experiment.

Our future work will investigate the three-dimensional transport process. In particular, Langmuir Circulation plays a significant role when considering mass and momentum transports in both the vertical and spanwise directions (Sanjou and Nezu 2014). We also aim to conduct further direct numerical simulations and 3D PIV measurements.

ACKNOWLEDGMENTS

The authors would like to thank the financial support of the Research Project Grant-In-Aid for Scientific Research (B) of Japanese Government (No. 19H02249, Principle Investigator: Y. Sugihara). Furthermore, we appreciate the editors and reviewers providing us with valuable comments and references.

AUTHOR DECLARATIONS

Conflict of Interest

The authors have no conflicts to disclose.

Author Contributions

Michio Sanjou: Conceptualization (equal); Formal analysis (equal); Investigation (equal); Writing – original draft (equal). **Yuji Sugihara:** Investigation (supporting); Methodology (supporting); Writing – review & editing (equal).

DATA AVAILABILITY

The data that support the findings of this study are available from the corresponding author upon reasonable request.

NOMENCLATURE

f_p	Peak frequency of wave fluctuation
H	Water depth
H_s	Significant wave height
u	Streamwise component of velocity fluctuation
$\tilde{u}$	Streamwise component of instantaneous fluctuation
U	Streamwise component of mean velocity
u_t	Streamwise component of turbulence
u_w	Streamwise component of wave motion
$U_{a,\max}$	Maximum wind velocity
U_s	Free-surface mean velocity
U_*	Friction velocity in the free-surface
$U^+ = (U_s - U)/U_*$	Mean streamwise velocity normalized by inner variables
v	Vertical component of velocity fluctuation
$\tilde{v}$	Vertical component of instantaneous fluctuation

ν	Kinematic viscosity
V	Vertical component of mean velocity
v_t	Vertical component of turbulence
v_w	Vertical component of wave motion
W	Spanwise component of mean velocity
x	Streamwise coordinate
y	Upward vertical coordinate, origin of which is flume bottom
y'	Downward vertical coordinate, origin of which is flume bottom
$y'+ = y'U_*/\nu$	Downward vertical coordinate normalized by inner variables
z	Spanwise coordinate

REFERENCES

Addona, F., Chiapponi, L., Clavero, M., Losada, M. A., and Longo, S., "On the interaction between partially-reflected waves and an opposing wind," Coastal Eng. **162**, 103774 (2020).

Addona, F., Lira Loarca, A., Chiapponi, L., Losada, M. A., and Longo, S., "The Reynolds wave shear stress in partially reflected waves," Coastal Eng. **138**, 220–226 (2018).

Auta, H. S., Emenike, C. U., and Fauziah, S. H., "Distribution and importance of microplastics in the marine environment: A review of the sources, fate, effects, and potential solutions," Environ. Int. **102**, 165–176 (2017).

Brach, L., Deixonne, P., Bernard, F. M., Durand, E., Desjean, E. C., Perez, E., van Sebille, E., and Ter Halle, L., "Anticyclonic eddies increase accumulation of microplastic in the North Atlantic subtropical gyre," Mar. Pollut. Bull. **126**, 191–196 (2018).

Cheung, T. K. and Street, R. L., "The turbulent layer in the water at an air-water interface," J. Fluid Mech. **194**, 133–151 (1988).

Chiapponi, L., Cobos, M., Losada, M. A., and Longo, S., "Cross-shore variability and vorticity dynamics during wave breaking on a fixed bar," Coastal Eng. **127**, 119–133 (2017).

Chiapponi, L., Addona, F., Diaz-Carrasco, P., Losada, M. A., and Longo, S., "Statistical analysis of the interaction between wind-waves and currents during early wave generation," Coastal Eng. **159**, 103672 (2020).

Clavero, M., Longo, S., Chiapponi, L., and Losada, M. A., "3D flow measurements in regular breaking waves past a fixed submerged bar on an impermeable plane slope," J. Fluid Mech. **802**, 490–527 (2016).

Colosimo, I., de Vet, P. L. M., van Maren, D. S., Reniers, A., Winterwerp, J. C., and van Prooijen, B. C., "The impact of wind on flow and sediment transport over intertidal flats," J. Mar. Sci. Eng. **8**(11), 910 (2020).

Deigaard, R. and Fredsoe, J., "Shear stress distribution in dissipative water waves," Coastal Eng. **13**, 357–378 (1989).

DiBenedetto, M. H., Ouellette, N. T., and Koseff, J. R., "Transport of anisotropic particles under waves," J. Fluid Mech. **837**, 320–340 (2018).

Farge, M., "Wavelet transforms and their applications to turbulence," Annu. Rev. Fluid Mech. **24**, 395–457 (1992).

Herlina, H. and Wissink, J. G., "Simulation of air-water interfacial mass transfer driven by high-intensity isotropic turbulence," J. Fluid Mech. **860**, 419–440 (2019).

Hussain, A. and Reynolds, W. C., "The mechanism of an organized wave in turbulent shear flow," J. Fluid Mech. **41**, 241–258 (1970).

Jiang, J. Y., Street, R. L., and Klots, S. P., "A study on wave-turbulence interaction by use of a nonlinear water wave decomposition technique," J. Geophys. Res. **95**, 16037–16054, https://doi.org/10.1029/JC095iC09p16037 (1990).

Kanhai, L. D. K., Officer, R., Lyashevska, O., Thompson, R. C., and O'Connor, I., "Microplastic abundance, distribution and composition along a latitudinal gradient in the Atlantic Ocean," Mar. Pollut. Bull. **115**(1–2), 307–314 (2017).

Kato, H., Nobuoka, H., and Ooshima, N., "Measurements of wind-driven current near the water surface by the use of the PTV method," *Gas Transfer at Water Surfaces*, Geophysical Monograph Series (American Geophysical Union, 2002), pp. 97–102.

Kukulka, T., Proskurowski, G., Moret-Ferguson, S., Meyer, D. W., and Law, K. L., "The effect of wind mixing on the vertical distribution of buoyant plastic debris," Geophys. Res. Lett. **39**, L07601, https://doi.org/10.1029/2012GL051116 (2012).

Law, K. L., "Plastics in the marine environment," Ann. Rev. Mar. Sci. **9**, 205–229 (2017).

Lin, S., Boegman, L., Valipour, R., Bouffard, D., Ackerman, J. D., and Zhao, Y., "Three-dimeensional modeling of sediment resuspension in a large shallow lake," J. Great Lakes Res. **47**(4), 970–984 (2021).

Longo, S., Chiapponi, L., Clavero, M., Makela, T., and Liang, D., "Study of the turbulence in the air-side and water-side boundary layers in experimental laboratory wind induced surface waves," Coastal Eng. **69**, 67–81 (2012b).

Longo, S., Clavero, M., Chiapponi, L., and Losada, M. A., "Invariants of turbulence Reynolds stress and of dissipation tensors in regular breaking waves," Water **9**(11), w9110893 (2017).

Longo, S., Liang, D., Chiapponi, L., and Jimenez, A., "Turbulent flow structure in experimental laboratory wind-generated gravity waves," Coastal Eng. **64**, 1–15 (2012a).

Mellor, G., "Pressure-slope momentum transfer in ocean surface boundary layers coupled with gravity waves," J. Phys. Oceanogr. **43**, 2173–2184 (2013).

Nielsen, P., Callaghan, D. P., and Baldock, T. E., "Downward transfer of momentum by wind-driven waves," Coastal Eng. **58**, 1118–1124 (2011).

Nove-Josserand, C., Perrard, S., Lozano-Duran, A., Benzaquen, M., Rabaud, M., and Moisy, F., "Effect of a weak current on wind-generated waves in the wrinkle regime," Phys. Rev. Fluids **5**, 124801 (2020).

Olfateh, M., Ware, P., Callaghan, D. P., Nielsen, P., and Baldock, T. E., "Momentum transfer under laboratory wind waves," Coastal Eng. **121**, 255–264 (2017).

Okamoto, T., Nezu, I., and Ikeda, H., "Vertical mass and momentum transport in open-channel flows with submerged vegetations," J. Hydro-Environ. Res. **6**(4), 287–297 (2012).

Pellini, G., Gomiero, A., Fortibuoni, T., Ferrà, C., Grati, F., Tassetti, N., Polidori, P., Fabi, G., and Scarcella, G., "Characterization of microplastic litter in the gastrointestinal tract of Solea solea from the Adriatic Sea," Environ. Pollut. **234**, 943–952 (2018).

Rashidi, M. and Banerjee, B., "The effect of boundary conditions and shear rate on streak formation and breakdown in turbulent channel flows," Phys. Fluids **2**, 1827–1838 (1990).

Rivero, F. J. and Arcilla, A. S., "On the vertical distribution of $\langle \tilde{u}\tilde{w} \rangle$," Coastal Eng. **25**, 137–152 (1995).

Sanjou, M., "Local gas transfer rate through the free surface in spatially accelerated open-channel turbulence," Phys. Fluids **32**, 105103 (2020).

Sanjou, M. and Nezu, I., "Secondary current properties generated by wind-induced water waves in experimental conditions," Adv. Oceanogr. Limnol. **5**(1), 1–17 (2014).

Sanjou, M. and Nezu, I., "Turbulent structure and coherent vortices in open-channel flows with wind-induced water waves," Environ. Fluid Mech. **11**(2), 113–131 (2011).

Sanjou, M., Nezu, I., and Okamoto, T., "Surface velocity divergence model of air/water interfacial gas transfer in open-channel flows," Phys. Fluids **29**, 045107 (2017).

Szeri, A. J., "Boundary layers at a dynamic interface: Air-sea exchange of heat and mass," J. Geophys. Res. **122**, 2781–2794, https://doi.org/10.1002/2016JC012312 (2018).

Thais, L. and Magnaudet, J., "Turbulent structure beneath surface gravity waves sheared by the wind," J. Fluid Mech. **328**, 313–344 (1996).

Tseng, C.-Y. and Tinoco, R. O., "A model to predict surface gas transfer rate in streams based on turbulence production by aquatic vegetation," Adv. Water Resour. **143**, 103666 (2020).

Wu, J., "Wind-induced drift current," J. Fluid Mech. **68**, 49–70 (1975).

Zainescu, F., van der Vegt, H., Storms, J., Nutz, A., Bozetti, G., May, J.-H., Cohen, S., Bouchette, F., May, S. M., and Schuster, M., "The role of wind-wave related processes in redistributing river-derived terrigenous sediments in Lake Turkana: A modelling study," J. Great Lakes Res. (in press) (2023).